Available online at www.sciencedirect.com
ScienceDirect
International Journal of Heat and Fluid Flow 27 (2006) 895–901
International Journal of HEAT AND FLUID FLOW
www.elsevier.com/locate/ijhff

Numerical simulation of compressible mixing layers

Song Fu *, Qibing Li

Department of Engineering Mechanics, Tsinghua University, Beijing 100084, China

Received 30 September 2005; received in revised form 16 February 2006; accepted 4 March 2006
Available online 30 June 2006

Abstract

Three-dimensional spatially developing compressible planar mixing layers are studied numerically for convective Mach number $M_c = 0.4$, 0.8 and 1.2. The present results for the flow-field structures, the mean velocity profiles, the mixing-layer growth rate and Reynolds stresses agree well with those of experiments and other numerical studies. The normalized growth rate decreases with increasing M_c. Shocklets are found to exist in the mixing layer at $M_c = 1.2$ and their formation mechanism shows good agreement with the scenario of flow around a bluff body. The effect of compressibility on the large-scale structures is stronger than that on the small-scale ones. The budget of the Reynolds-stress transport equations agree well with that from the temporal developing results. The magnitudes of most of the contributing terms in the budget reduce with increased compressibility effect except for the pressure-dilatation term which is very small.

Keywords: Numerical simulation; Spatially developing mixing layer; Compressibility; Shocklets; Budget of transport equation

1. Introduction

The compressible mixing layer has been a research focal point in recent years for its distinct turbulent characteristics unknown in incompressible case (Vreman et al., 1996; Pantano and Sarkar, 2002; Kourta and Sauvage, 2002; Goebel and Dutton, 1991; Debisschop et al., 1994; Barre et al., 1997; Rossmann et al., 2002; Gutmark et al., 1995). A well-known feature is that the normalized growth rate of the mixing layer decreases rapidly with increasing convective Mach number M_c defined as the ratio of the free-stream velocity difference to the sum of the sound speeds. The mixing layer also becomes highly three-dimensional in contrary to the Brown–Roshko type vortices (Brown and Roshko, 1974) seen in low-speed mixing layer. The normalized turbulent quantities also decrease in magnitude with the increase in M_c. In the high-M_c mixing layers there exist unsteady shocklets that require high fidelity numerical scheme to capture.

Due to the limitation of computer capability, many of the existing numerical simulations of the compressible mixing layer are in two-dimensional (2D) or of temporal development in which the periodic conditions are applied in the streamwise direction. While the temporal simulations are computationally efficient, spatially evolving simulations can resolve more flow physics. In the present work the three-dimensional (3D) spatially developing compressible mixing layers, with M_c ranging from 0.4 to 1.2, are investigated numerically with the simplified gas-kinetic BGK scheme (Li and Fu, 2005; Li et al., 2005). The scheme is based on the BGK-Boltzmann equation and has been found with good performance in a wide rage of application, especially in viscous compressible flows (Xu, 2001; Xu et al., 2005). The aim is to further elucidate the fascinating flow structures as M_c increases.

2. Computational parameters

In the present study, the same grid system of uniformly spaced in the x and z direction and stretched in the y direction is employed for the three cases. The computational

* Corresponding author.
E-mail address: fs-dem@mail.tsinghua.edu.cn (S. Fu).

0142-727X/$ - see front matter © 2006 Elsevier Inc. All rights reserved.
doi:10.1016/j.ijheatfluidflow.2006.03.028

Table 1
Computational parameters

Case	M_1	M_2	M_c	Re_c	Re	Re_λ	M_t	L_η	δ_m
1	1.9	1.1	0.4	375	200	319	0.21	0.060	3.14
2	2.9	1.3	0.8	525	400	488	0.36	0.044	3.35
3	3.5	1.1	1.2	575	600	641	0.49	0.040	3.51

domain size is defined as $L_x \times L_y \times L_z = 350 \times 120 \times 30$ with $N_x \times N_y \times N_z = 875 \times 200 \times 80$ grid points. The ratio of the maximal cell size to the minimal size ($\Delta y_{min} = 0.2$) is 10.5. All variables are non-dimensionalized by the initial vorticity thickness $\delta_\omega(0)$ and the free stream parameters $\rho_1, a_1, \rho_1 a_1^2$ at the high-speed side. The initial momentum thickness can be calculated as $\delta_m(0) = 0.25$ for the velocity profile given by the hyperbolic tangential function. The free stream sound speed is set to $a_1 = a_2 = 1$, and pressure $p_1 = p_2 = 1/\gamma$, where gas constant $\gamma = 1.4$. The kinematic viscosity $v = 0.001$ and the Prandtl number $Pr = 1$ are adopted for all of the computations. Table 1 provides the parameters of three computational cases where Re_c and Re are the Reynolds numbers based on $U_c = (U_1 + U_2)/2$ and $\Delta U = U_1 - U_2$ respectively. In order to compare with other existing studies, here the momentum thickness is adopted to evaluate Reynolds numbers. Additionally, the integrated momentum thickness varies more smoothly along the streamwise direction, thus it is also used to normalize some results. The present computational domains are large enough for the flow to achieve fully developed state, as when $x = L_x$, x_{eff}/δ_{m1} are all larger than 1500, where $x_{eff} = x(1 - U_2/U_1)$, δ_{m1} is the momentum thickness of the high-speed stream set to half of the total thickness here. The criterion for $x_{eff}/\delta_{m1} > 500$ was proposed by Papamoschou and Roshko (1988). The last four columns in Table 1 summarizes the values of the key non-dimensional parameters calculated at the downstream location of the mixing-layer center ($x = 320$). The Kolmogorov scale L_η and the micro-scale Reynolds number Re_λ are defined as $L_\eta = (v^3/\varepsilon)^{0.25}$, $Re_\lambda = q^2\sqrt{5/v\varepsilon}$, where $q^2 = \overline{u'^2} + \overline{v'^2} + \overline{w'^2}$ is twice the turbulent kinetic energy. The Reynolds numbers are large enough for turbulence to occur. In all the three cases, the minimal cell size 0.2 is somewhat larger than the Kolmogorov scale, turbulent dissipation may not be well resolved. Thus Taylor Reynolds numbers seem to be overpredicted, when compared with the results of Pantano and Sarkar (2002). However, the quantities associated with large-scale structures are of the major concern here. The present gas-kinetic BGK scheme is second-order accurate both in spatial and temporal directions, and the collision time is related to the viscosity, $\tau = \mu/p$. The computational time step Δt is calculated with Courant number $CFL = 0.6$, which is always larger than the collision time in the present study.

At the inflow boundary ($i = 1$), the flow quantities, such as density, velocity, and pressure are prescribed, a broadband forcing (Stanley and Sarkar, 1997) with random phase shift in the spanwise direction is also superimposed at the inlet to generate the early development of the shear layer. For the outflow and the two lateral side boundaries Thompson's non-reflecting boundary conditions are employed and the pressure correction proposed by Poinsot and Lele (1992) is also applied at the outflow boundary. The streamwise velocity profile of the inflow is given by the hyperbolic tangential function. The simulation is started with an initialized flow field in which the streamwise velocity is determined by the inflow profile and the transverse velocity is fixed at zero value. The density and pressure fields are uniform throughout the flow field.

A test case is calculated with the same parameters as case 1 except for the coarser computational mesh to examine the level of grid dependency. The cell size is about one and a half times larger than that in case 1. Fig. 1 shows the comparisons of the coarse and fine grid results at different streamwise locations. The mean streamwise results with different computational mesh vary little showing the present grid mesh adequate in resolving the flow features.

3. Results

3.1. Flow structures and shocklets

In a lower M_c mixing layer such as the case 1, the typical vortex pairing can be observed from the iso-surface of the pressure p, the second invariant Q of the velocity gradient tensor ($\nabla\mathbf{u}$) as well as the second largest eigenvalue, λ_2, of $\mathbf{S}^2 + \mathbf{\Omega}^2$ where $\mathbf{S}$ and $\mathbf{\Omega}$ are the symmetric and antisymmetric components of $\nabla\mathbf{u}$. The present results verified the conclusion of (Jeong and Hussain, 1995) that in most cases the Q- and λ_2-definitions of a vortex are similar. Fig. 2 shows the isosurfaces of λ_2 in the mixing layer with $M_c = 0.4$ and $M_c = 1.2$. It is seen there that the mixing at $M_c = 0.4$ has similar vortex evolution patterns to the incompressible flow, changing from spanwise roller to the so called 'helical pairing' and then to turbulence. The 'ribs' can be clearly seen between the rollers. For the mixing layer with $M_c = 1.2$, oblique structures occur in the upstream region of instability. The structures related to pressure can be better identified through the isosurfaces of pressure at high M_c, although they can hardly describe the small structures such as the 'ribs' for the low-M_c cases.

The information of vortex evolution can be further found from the energy spectrum. Fig. 3 shows the power spectrum of streamwise velocity along the geometric centerline ($y = 0$). Here the Strouhal number is defined as $St = f\delta_m(0)/U_c$. Wide range spectrum, can be seen in the figure suggesting that the mixing layer has become fully developed turbulent flows. The short range with spectral slope $-5/3$ comes from the low Reynolds number of the present flow. In the mixing layers with different M_c, the streamwise velocity spectra are similar except for the peak positions in the low-frequency part. That is, compressibility mainly affects large-scale fluctuations.

From the distribution of the density and streamwise velocity shown in Fig. 4, the strong discontinuity around

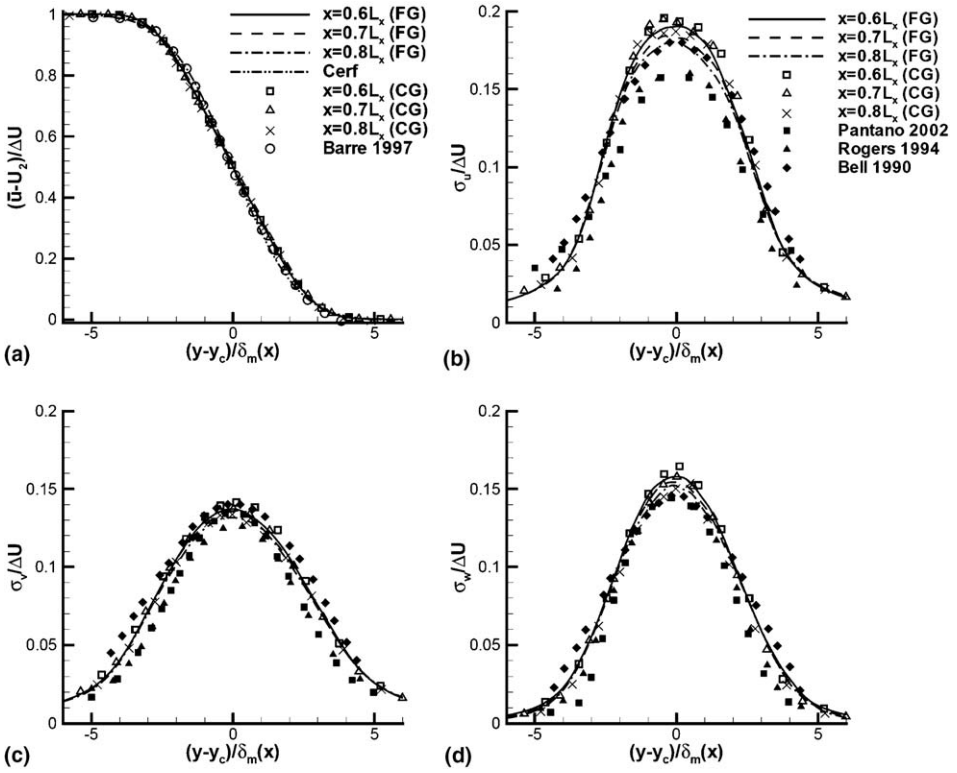

Fig. 1. Profiles of the mean streamwise velocity (a) and the velocity fluctuation intensity (b–d) at different locations (Case 1). 'Cerf' is the error function profile which is the first-order approximation to the mean streamwise velocity in incompressible mixing layer. The symbol 'FG' represents the results calculated on the fine grid and 'CG' on the coarse grid. The legends are the same in (b–d).

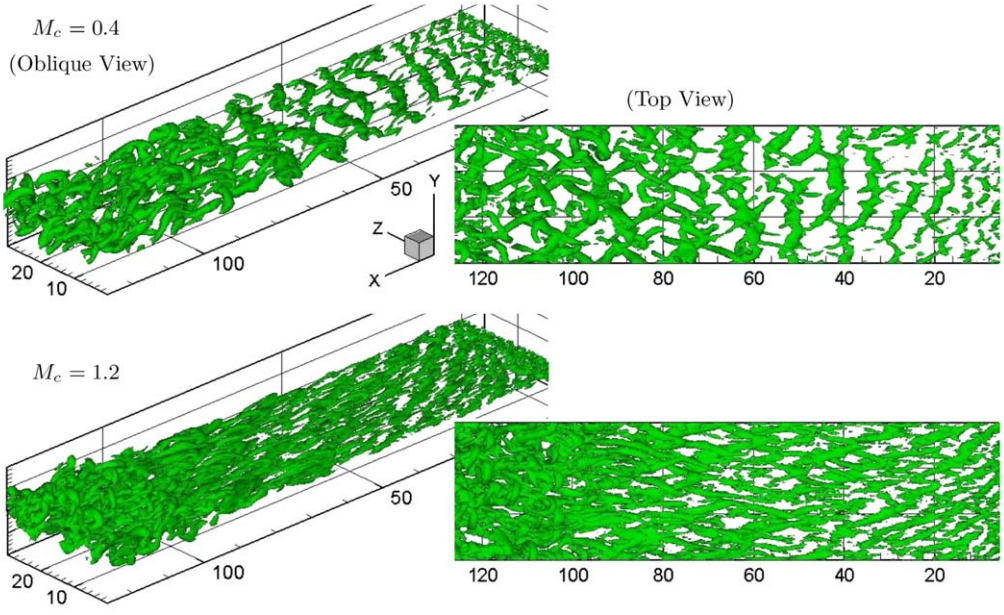

Fig. 2. Isosurfaces of λ_2 ($\lambda_2 = -0.01$).

the low-speed fluid engulfed into the high-speed can be clearly seen. These discontinuities show good similarity with the flow around a bluff body. Although the present calculated shocklets are rather straight, more like oblique shocks, due to relatively low-convective Mach number, the present numerical images agree with Rossmann's experimental results, thus verifying the model of shock formation.

To further study the shocklets in the mixing layer, one must identify the location of a shock. A good method is

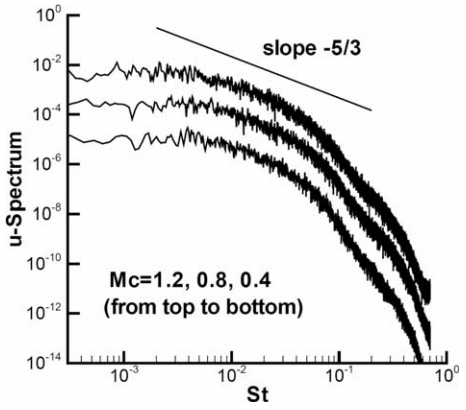

Fig. 3. Spectra of the streamwise velocity in the inner region of the mixing layers ($x = 0.8L_x$, $y^* = (y - y_c)/\delta_m = 0.2, -0.7, -0.4$, respectively) for different M_c. For clarity, the spectra are divided by the factors: 10 for $M_c = 0.8$ and 100 for $M_c = 0.4$.

to check the entropy of the fluid moving across the discontinuity through tracking the fluid particles. In view of the complex flow structure and large amount of computational data for the three-dimensional flow, a much simpler method is adopted here. Since a shock corresponds to a large pressure difference in the direction perpendicular to the shock, the existence of shock is verified in three ways: (1) the pressure gradient field ∇p is examined to find the locations with high peaks; (2) the dilatation $\nabla \cdot \mathbf{u}$ is checked for large negative values as shocks lead to a strong compression of the fluid; (3) the densities on both sides of these jump interface with three or four cells size are checked with Rankine–Hugoniot (R–H) relations. If an interface satisfies these three verifications, it is deemed as a shock and the maximal pressure gradient direction is the shock orientation. Fig. 5 shows two of these. shocks whose orientations are nearly perpendicular to the spanwise direction. The pressures besides them are $(p_1, p_2) = (0.55809, 0.90895)$ and $(0.62775, 0.79097)$, and the densities $(\rho_1, \rho_2) = (0.75623, 1.1688)$ and $(0.91172, 1.0748)$. The pressure jumps are thus 1.63 and 1.26 and are identified with dashed circles in the figure. The deviations from the R–H relation are 9% and nearly zero, respectively. Furthermore, the velocity vectors shown in Fig. 5 indicate that they are oblique shocks, corresponding to stationary inviscid shocks with Mach numbers $M = 1.3$ and 1.6, with oblique angles $\beta = 75°$ and 43°, respectively. Here the angle is defined based on the shape of a shock and the direction of the local flow. It should be noted that although these two shocks are almost parallel, the directions of the local upstream flow are quite different.

It is further noted that the shocklets in the mixing layer have complex structures in three dimensions. The effects of the numerical scheme, the boundary and initial conditions, the size of the computational domain, and the lack of effective criterion to identify the shock, as well as the complexity of three-dimensional flow structure lead to the difficulties in the shocklets identification among different studies (Vreman et al., 1996). For the experimental investigations on the existence of shocklets very powerful visualization and measurement techniques are required (Papamoschou, 1995; Alvi et al., 1996; Rossmann et al., 2002).

3.2. Statistics and compressibility

The turbulence statistics is obtained in about six times of the maximal time scale $T = L_x/U_c$. Fig. 6 shows the development of the mixing layers where one can see that the mixing layer reaches linear region after some distance from the upstream and the center of the mixing layer leads to the low-speed side. This feature is observed in experiments but can not be captured in the numerical simulations of temporally developing mixing layer. With increasing convective Mach number, the mixing layer shows more stable, thus

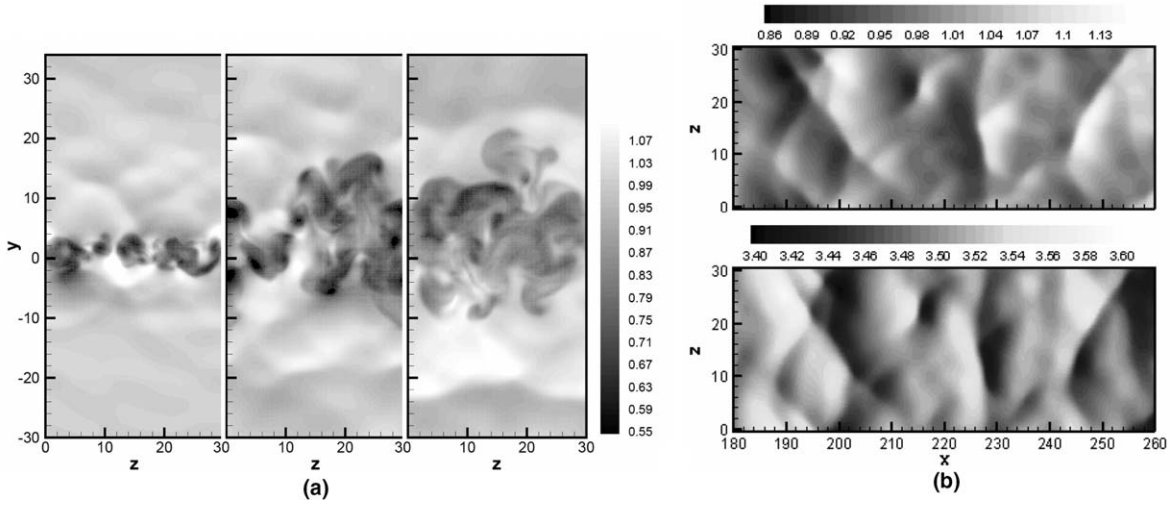

Fig. 4. Instantaneous flow fields at different streamwise and transverse planes. (a) Density contours at $x = L_x/3$, $x = 2L_x/3$ and $x = L_x$, respectively; (b) contours at $y = -14$, top picture denotes to density and the bottom for the streamwise velocity.

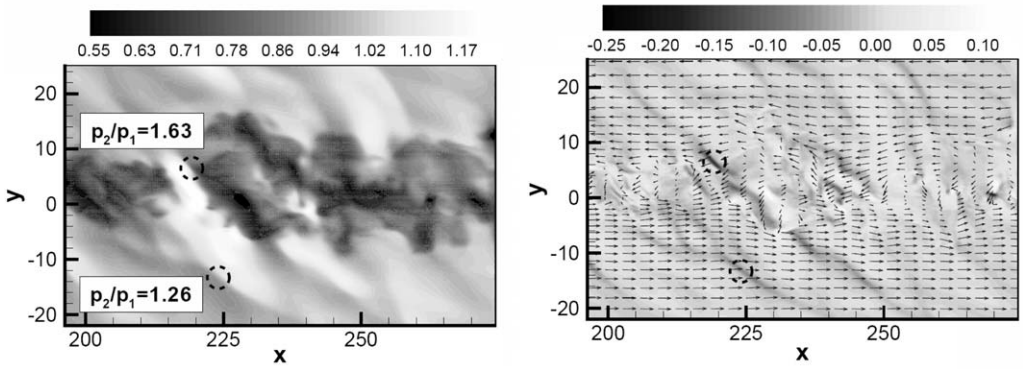

Fig. 5. The instantaneous density fields (left), divergence $\nabla \cdot \vec{u}/(\Delta U/\delta_\omega(0))$ fields with velocity fields (right) on a spanwise plane ($M_c = 1.2$, $z = 15$). The mean convective velocity $U_c\vec{i}$ is subtracted from the velocity fields.

much longer streamwise distance is required for the flow to develop turbulence.

The normalized growth rates (shown in Fig. 7) calculated from the momentum thickness in the fully developed region decrease evidently with increasing M_c which agrees with existing data (Papamoschou and Roshko, 1988; Rossmann et al., 2002; Goebel and Dutton, 1991; Debisschop et al., 1994; Samimy and Elliott, 1990) and the numerical results (Freund et al., 2000; Kourta and Sauvage, 2002). The normalizing factor δ'_{m0}, the growth rate for incompressible mixing layer, is set 0.04 indicating the corresponding vorticity thickness growth rate to be $\delta'_{\omega 0} = 0.18$ or 0.16 if the mean streamwise velocity profile is an error function or a hyperbolic tangent, respectively. The peak linear mode amplification rate, which has been shown to be highly correlated to the spreading rates (Ragab and Wu, 1989; Sandham and Reynolds, 1990), calculated by Day et al. (1998) for spatially developing plane mixing layers, is also shown in this figure and is suppressed more rapidly than the present results. The data in this figure exhibit significant scattering that is partly attributed to the different experimental conditions and partly to the different mixing-layer thickness definitions adopted by various authors, calculating the growth from the momentum, the vorticity thickness, or the mean pressure fields.

Different developing regions can also be found in Fig. 8, where k_i is the integration of the fluctuation energy along

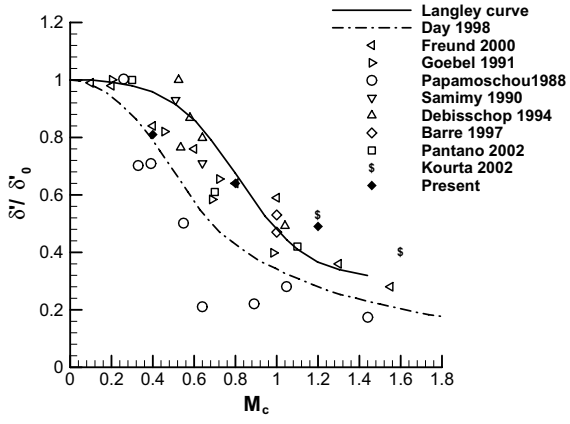

Fig. 7. Normalized growth rates of different M_c mixing layer.

the transverse direction. σ_{uv} is the mean square root of the shear stress. The locations where k_i changes significantly are similar to that of δ_m, but behind that of the maximum Reynolds stresses. In low-M_c mixing layer, the shear stress achieves its maximum earlier than the other Reynolds-stress components. In high-M_c mixing layer, three evolution stages can be observed more clearly and the streamwise Reynolds stress component reaches its

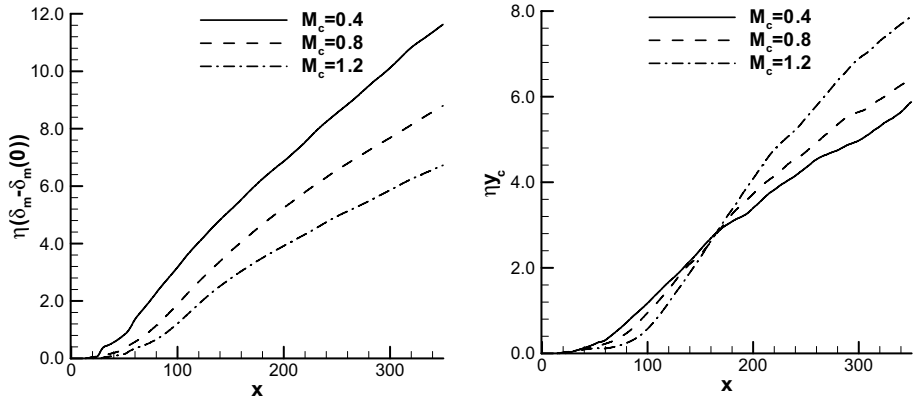

Fig. 6. Development of mixing layers with different M_c. Left is the normalized momentum thickness and right the center of mixing layer.

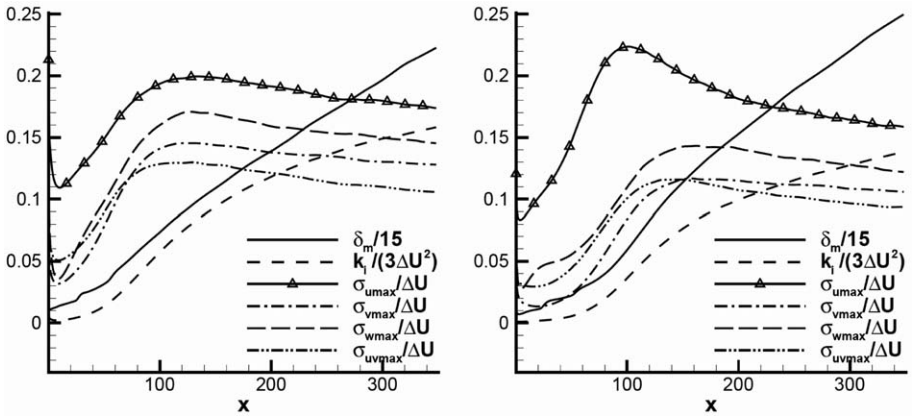

Fig. 8. Evolution of the maximum velocity fluctuation compared with the momentum thickness and the integrated turbulent energy in the mixing layer with $M_c = 0.4$ (left) and $M_c = 1.2$ (right).

maximum value first but then decrease quickly. These agree with the fact that turbulent energy is generated mainly in the streamwise direction through the interaction of the shear stress and the streamwise velocity gradient, $-\overline{uv}\partial U/\partial y$. The streamwise component of the turbulence energy is then redistributed to the other two components. In high-M_c flow, the compressibility inhibits turbulent energy redistribution from streamwise to transverse and spanwise directions, thus the streamwise component remains large for a significant distance. These trends agree with the DNS results of Pantano and Sarkar (2002) for temporally developing compressible mixing layers. However the experimental measurement (Elliott and Samimy, 1990; Goebel and Dutton, 1991) showed a more dramatic decrease of the transverse velocity fluctuation $\sigma_{vmax}/\Delta U$ with a factor of about two between $M_c \approx 0$ and $M_c \approx 1$.

3.3. Budget of Reynolds stress transport

To further understand the compressibility effects on turbulence, the budgets of Reynolds-stress transport are evaluated. Here the Favre averaged transport equations are considered,

$$\partial\tau_{ij}/\partial t = C_{ij} + P_{ij} + D_{ij} + \Pi_{ij} + \varepsilon_{ij} + M_{ij} \tag{1}$$

where the Reynolds stresses τ_{ij}, the convection term C_{ij}, the production term P_{ij}, the pressure–strain term Π_{ij}, the dissipation term ε_{ij}, and the mass flux term M_{ij} are defined as,

$$\begin{cases} \tau_{ij} = \overline{\rho u_i'' u_j''}, \quad C_{ij} = -(\tilde{u}_k \overline{\rho u_i'' u_j''})_{,k}, \quad P_{ij} = -\overline{\rho u_i'' u_k''}\tilde{u}_{j,k} - \overline{\rho u_j'' u_k''}\tilde{u}_{i,k} \\ \Pi_{ij} = \overline{p' u_{i,j}'} + \overline{p' u_{j,i}'}, \quad \varepsilon_{ij} = -\overline{\sigma_{ik}' u_{j,k}'} - \overline{\sigma_{jk}' u_{i,k}'}, \\ M_{ij} = \overline{u_i''}\bar{p}_{,j} + \overline{u_j''}\bar{p}_{,i} - \overline{u_i''}\bar{\sigma}_{jk,k} - \overline{u_j''}\bar{\sigma}_{ik,k} \\ D_{ij} = D_{ij}^{v} + D_{ij}^{t} + D_{ij}^{p} \\ \quad = (\overline{u_j'\sigma_{ik}'} + \overline{u_i'\sigma_{jk}'})_{,k} - (\overline{\rho u_i'' u_j'' u_k''})_{,k} - (\overline{p' u_i'}\delta_{jk} + \overline{p' u_j'}\delta_{ik})_{,k} \end{cases} \tag{2}$$

The diffusion term D_{ij} includes three parts, the viscous diffusion, the turbulence diffusion and the pressure diffusion. The reminder from Eq. (1) is represented by Er_{ij} to study the accuracy of balance.

Fig. 9(a) shows the budget of shear stress transport in the fully developed region of the mixing layer with $M_c = 0.4$, where all the terms are normalized with $\Delta U^3/\delta_m(x)$. The distributions of most of the terms agree with the temporal developing simulations of Pantano and Sarkar (2002) and the budget error can be seen small indeed.

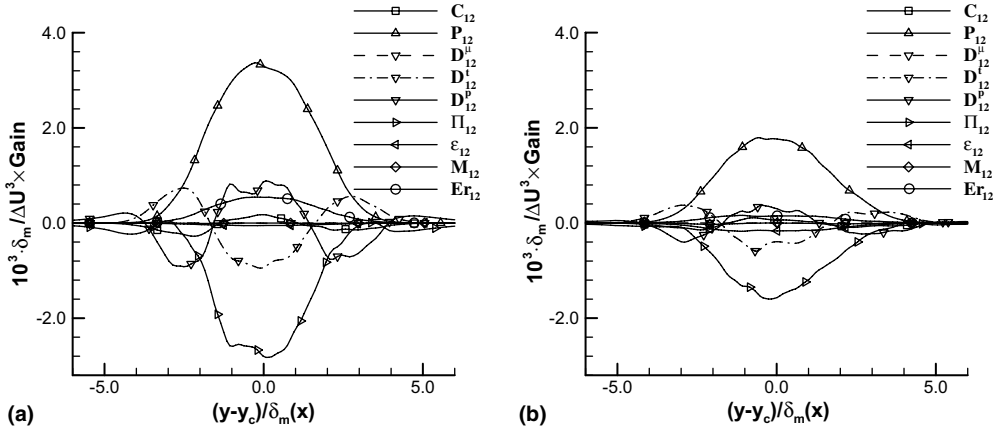

Fig. 9. Budgets of Reynolds stress transport at the location about $x = 0.6L_x$ of the mixing layers with $M_c = 0.4$ (a), and 1.2 (b).

As mentioned above, the turbulence dissipation may not be accurately captured with the present computational mesh, but Reynolds shear stress is dominated by large-scale structures, thus good balance can be obtained. Fig. 9 also tell us that the budget of the shear stress is dominated by the production term and the pressure–strain term. The pressure diffusion and turbulence diffusion are much smaller. Different to the production term, the pressure–strain correlation term is negative throughout the mixing layer, acting as the dissipation term. The dissipation term can also be seen inherent small. With increasing M_c, the value of each term decreases (Fig. 9b), so does that in the turbulent energy budget except for the pressure-dilatation term although it is still very small. The decrease of each term in the budget with increasing M_c is consistent with the previous studies that the reduction of the pressure–strain correlation not only inhibits the transport of the turbulence energy from the streamwise direction to the transverse direction, but also decreases the production of the turbulence energy, resulting in the decrease of the growth rate of the mixing layer (Pantano and Sarkar, 2002).

4. Conclusion

Three-dimensional spatially developing planar compressible mixing layer at $M_c = 0.4$, 0.8 and 1.2 are studied numerically. The present results agree well with the experimental and other numerical results. Shocklets are found in the mixing layer at $M_c = 1.2$. It is elucidated here that the shocklets are formed in the mixing layer when lumps of low-speed fluid enter the high-speed flow, i.e., it is in a way similar as the supersonic flow around a bluff body. The effect of compressibility on the large-scale structures is stronger than that on the small-scale ones. The magnitudes of most of the contributing terms in the budget reduce with increased compressibility effect.

Acknowledgements

This work is supported by the National Natural Science Foundation of China (10302015, 10232020) and the National Key Basic Research Special Funds of China (2001CB409600).

References

Alvi, F.S., Krothapalli, A., Washington, D., 1996. Experimental study of a compressible countercurrent turbulent shear layer. AIAA J. 34, 728–735.

Barre, S., Braud, P., Chambres, O., Bonnet, J.P., 1997. Influence of inlet pressure conditions on supersonic turbulent mixing layers. Exp. Therm. Fluid Sci. 14, 68–74.

Brown, G.L., Roshko, A., 1974. On density effects and large structures in turbulent mixing layers. J. Fluid Mech. 64, 775–816.

Day, M.J., Reynolds, W.C., Mansour, N.N., 1998. The structure of the compressible reacting mixing layer: insights from linear stability analysis. Phys. Fluids 10, 993–1007.

Debisschop, J.R., Chambres, O., Bonnet, J.P., 1994. Velocity field characteristics in supersonic mixing layer. Exp. Therm. Fluid Sci. 9, 147–155.

Elliott, G.S., Samimy, M., 1990. Compressibility effects in free shear layers. Phys. Fluids A 2, 1231–1240.

Freund, J.B., Lele, S.K., Moin, P., 2000. Compressibility effects in an turbulent annular mixing layer: Part 1. Turbulence and growth rate. J. Fluid Mech. 421, 229–267.

Goebel, S.G., Dutton, J.C., 1991. Experimental study of compressible turbulent mixing layers. AIAA J. 29, 538–546.

Gutmark, E.J., Schadow, K.C., Yu, K.H., 1995. Mixing enhancement in supersonic free shear flows. Annu. Rev. Fluid Mech. 27, 375–471.

Jeong, J., Hussain, F., 1995. On the identification of a vortex. J. Fluid Mech. 285, 69–94.

Kourta, A., Sauvage, R., 2002. Computation of supersonic mixing layers. Phys. Fluids 14, 3790–3797.

Li, Q.B., Fu, S., 2003. Numerical simulation of high-speed planar mixing layer. Comput. Fluids 32, 1357–1377.

Li, Q.B., Fu, S., Xu, K., 2005. A compressible Navier–Stokes flow solver with scalar transport. J. Comput. Phys. 204, 692–714.

Pantano, C., Sarkar, S., 2002. A study of compressibility effects in the high-speed turbulent shear layer using direct simulation. J. Fluid Mech. 451, 329–371.

Papamoschou, D., 1995. Evidence of shocklets in a counterflow supersonic shear layer. Phys. Fluids 7, 233–235.

Papamoschou, D., Roshko, A., 1988. The compressible turbulent shear layer: an experimental study. J. Fluid Mech. 197, 453–477.

Poinsot, T.J., Lele, S.K., 1992. Boundary conditions for direct simulations of compressible viscous flows. J. Comput. Phys. 101, 104–129.

Ragab, S.A., Wu, J.L., 1989. Linear instability in two-dimensional compressible mixing layers. Phys. Fluids A 1, 957–966.

Rossmann, T., Mungal, M.G., Hanson, R.K., 2002. Evolution and growth of large-scale structures in high compressibility mixing layers. J. Turbulence 3, 009.

Samimy, M., Elliott, G.S., 1990. Effects of compressibility on the characteristics of free shear layers. AIAA J. 28, 439–445.

Sandham, N.D., Reynolds, W.C., 1990. Compressible mixing layer: linear theory and direct simulation. AIAA J. 28, 618–624.

Stanley, S., Sarkar, S., 1997. Simulations of spatially developing two-dimensional shear layers and jets. Theor. Comput. Fluid Dyn. 9, 121–147.

Vreman, A.W., Sandham, N.D., Luo, K.H., 1996. Compressible mixing layer growth rate and turbulence characteristics. J. Fluid Mech. 320, 235–258.

Xu, K., 2001. A gas-kinetic BGK scheme for the Navier–Stokes equations, and its connection with artificial dissipation and Godunov method. J. Comput. Phys. 171, 289–335.

Xu, K., Mao, M., Tang, L., 2005. A multidimensional gas-kinetic BGK scheme for hypersonic viscous flow. J. Comput. Phys. 203, 405–421.